Magnetic order and ferroelectricity in $RMnO_3$ multiferroic manganites: coupling between R- and Mn-spins



2008 J. Phys.: Condens. Matter 20 434215

(http://iopscience.iop.org/0953-8984/20/43/434215)

J. Phys.: Condens. Matter **20** (2008) 434215 (12pp) doi:10.1088/0953-8984/20/43/434215

# Magnetic order and ferroelectricity in $RMnO_3$ multiferroic manganites: coupling between R- and Mn-spins

**N Aliouane[1], O Prokhnenko[1], R Feyerherm[1], M Mostovoy[2], J Strempfer[3], K Habicht[1], K C Rule[1], E Dudzik[1], A U B Wolter[1], A Maljuk[1] and D N Argyriou[1,4]**

[1] Hahn-Meitner-Institut, Glienicker Strasse 100, D-14109 Berlin, Germany
[2] Zernike Institute for Advanced Materials, University of Groningen, 9747 AG Groningen, Netherlands
[3] Hamburger Synchrotronstrahlungslabor (HASYLAB) at Deutsches Elektronensynchrotron (DESY), 22605 Hamburg, Germany

E-mail: argyriou@hmi.de

Received 18 March 2008, in final form 16 June 2008
Published 9 October 2008
Online at stacks.iop.org/JPhysCM/20/434215

**Abstract**

Combining polarized and unpolarized neutron scattering techniques with x-ray resonant magnetic scattering we have studied the coupling between the Mn- and R-spin-ordering in the multiferroic $RMnO_3$, R = Tb and Dy. Polarized neutron diffraction reveals the moment orientation associated with the various modes describing the complex magnetic ordering observed in $TbMnO_3$, while neutron diffraction in high magnetic fields allows the identification of the origin (Mn versus Tb) of the various modes. In this way we identify significant $C_x$ and $F_z$ contributions from Tb arising from the coupling of Tb moments to the Mn cycloidal ordering. The x-ray studies give further insight into this coupling. In the ferroelectric phase, both $TbMnO_3$ and $DyMnO_3$ show an induced ordering of the R-ion with a propagation vector clamped to the Mn ordering. While in $TbMnO_3$ this clamping leads to a ground state in which the two propagation vectors $\tau^{Tb}$ and $\tau^{Mn}$ obey the relation $3\tau^{Tb} - \tau^{Mn} = 1$, in $DyMnO_3$ the ferroelectric polarization is effectively enhanced. The theoretical analysis of these effects not only explains the observed behavior for R = Tb and Dy but can also be applied to understand the Mn–R interaction in the related compounds with R = Gd and Ho. Finally we show both experimentally and theoretically how the Mn–R coupling can enhance the ferroelectric polarization in this manganite's multiferroics.

(Some figures in this article are in colour only in the electronic version)

## 1. Introduction

How to create strong coupling between different types of ferroic order is a long standing issue in modern condensed matter physics [1]. While there are numerous technological applications for magnets and ferroelectrics, to strongly couple them in a single material has been the aim of technological as well as scientific pursuit. While the linear magneto-electric effect was realized in the 1960s, the work that followed failed to deliver materials that exhibited a strong magneto-electric coupling [1, 2]. For example ferroelectric magnets such as $BaMnF_4$, where the ferroelectric and magnetic transitions are separated by hundreds of degree Kelvin, showed little or no evidence of magneto-electric coupling [3]. This behavior from ferroelectric magnets led to the conclusion that magneto-electric coupling is intrinsically very weak and that ferroelectricity and magnetism tend to avoid each other [1, 2].

This conclusion was recently remarkably proved to be wrong with the discovery of a novel mechanism leading to multiferroicity: *frustration* [4]. Systems with competing magnetic interactions show many types of novel magnetic

[4] Author to whom any correspondence should be addressed.

 

ordering. The result is a set of materials with spectacular properties such as giant magneto-capacitance [5], magnetically induced electric polarization flops [6, 7], and a rotation of electric polarization in a periodically varying magnetic field [8, 9]. These developments not only put the old conjecture on the size of the coupling in magneto-electrics into an entirely different perspective but also they have revitalized efforts to discover new magneto-electric materials and understand the origin of their properties.

Magnetic frustration in $RMnO_3$ perovskite manganites, where R is a trivalent rare earth, can be induced by structural tuning of the nearest ($J_1$) and next nearest ($J_2$) Mn magnetic interactions [10]. The variation of the size of the R-ion directly varies the Mn–O–Mn bond angles and modulates the strength of the super-exchange interaction between Mn-ions. In $LaMnO_3$ the antiferro-type ordering of singly occupied $Mn^{3+}$ $3d_{3x^2-r^2}$ and $3d_{3y^2-r^2}$ orbitals produces ferromagnetic (FM) interactions within the $ab$-plane of the perovskite lattice (A-type magnetic structure) while the coupling between planes is antiferromagnetic (AFM). As the size of the trivalent R cation decreases, the A-type phase becomes frustrated. This is highlighted by the steady decrease of $T_N$ from 150 K for R = La to ∼40 K for R = Eu [10]. This behavior, which is ascribed to progressive weakening of $J_2$ with respect to $J_1$ [10–12], leads to a commensurate AFM ordering within the $ab$-plane of the perovskite lattice for R = Ho (E-type magnetic structure) [13]. For compounds in the intermediate region of R = Gd, Tb and Dy [5, 6], commensurate AFM ordering is not stable and the competition between the strengths of $J_1$ and $J_2$ leads to an incommensurate cycloidal magnetic structure whose most prominent feature is the breaking of inversion symmetry [4]. Although the size of the polarization is relatively small (∼0.05 $\mu C\,m^{-2}$) compared to proper ferroelectrics, this new way of generating a strong magneto-electric coupling leads to materials where the ferroelectric polarization can be controlled directly by a magnetic field [7]. For R = Tb and Dy the direction of the ferroelectric polarization can be flopped from the $c$-axis to the $a$-axis with a magnetic field applied along the $a$- and $b$-direction [7], while for R = Gd ferroelectricity can be induced with a magnetic field applied parallel to the $b$-axis [5].

The magnetic ordering in the R = Tb, Dy perovskites exhibits three distinctive transitions. The first occurs at $T_N \sim 41$ K where Mn-spins order in a longitudinal spin-density wave (SDW) propagating along the $b$-direction and with wavevector $\tau^{Mn} \approx 0.27\mathbf{b}^*$ (see figure 1(a)) [14, 15]. The second transition occurs at $T_S = 28$ K for R = Tb and 18 K for R = Dy, and here Mn-spins develop a component along the $c$-axis that has a phase difference of $\pi/2$ compared to the $b$-axis component, thus resulting in a cycloidal Mn-spin order as shown in figure 1(b). Indeed it is below $T_S$ where a spontaneous polarization along the $c$-axis develops [7]. On further cooling for R = Tb a final transition occurs at $T_N^{Tb} = 7$ K where Tb-spins order independently with $\tau^{Tb} \sim 0.42\mathbf{b}^*$ [14], while for R = Dy below $T_N^{Dy} = 6.5$ K, Dy-spins order commensurately with $\tau^{Dy} = (1/2)\mathbf{b}^*$ [16].

Ferroelectricity in these frustrated manganites results from the antisymmetric Dzyaloshinski–Moriya (DM) interaction

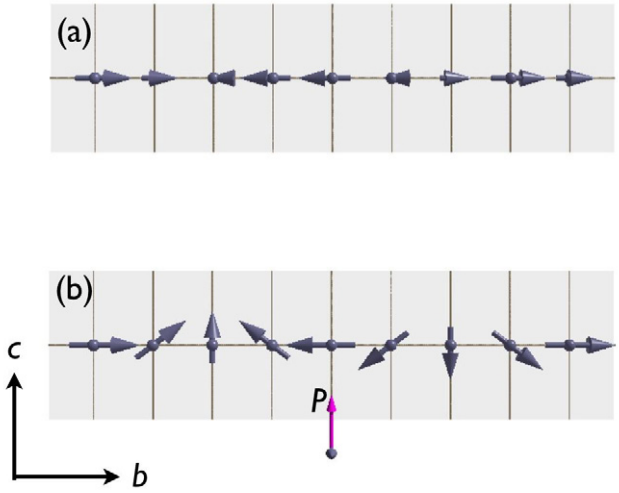


**Figure 1.** Ordering of Mn-spins in multiferroic $TbMnO_3$ in (a) the high temperature SDW phase below $T_N = 41$ K and (b) in the ferroelectric cycloidal phase below $T_S = 28$ K. In the latter the cycloidal ordering is elliptical with $\mu_z \sim 3/4\mu_y$.

which is a relativistic correction to the usual super-exchange and its strength is proportional to the spin–orbit coupling constant [4]. The DM interaction between two spins, $S_i$, $S_j$ separated by $r_{ij}$ is defined as $r_{ij} \times S_i \times S_j$ and favors non-collinear spin-ordering such as cycloids or helices. The spontaneous ferroelectric polarization, $\mathbf{P}_s$, can be expressed in terms of parameters that characterize the spin cycloid, namely, $\mathbf{P}_s \propto m_y m_z(\mathbf{e_x} \times \boldsymbol{\tau})$, where $m_y$ and $m_z$ are the amplitude of the spins along the $b$- and $c$-axis respectively, $\mathbf{e_x}$ is a unit vector along the axis of rotation of Mn-spins and $\boldsymbol{\tau}$ is the magnetic propagation vector [15, 17, 18]. This phenomenological description as well as the theoretical framework based on the spin-current model has been very successful in predicting the size and direction of the polarization in the multiferroic manganites. For example for R = Tb, the propagation vector is along the $b$-axis while Mn-spins rotate around the $a$-axis, predicting a spontaneous polarization parallel to the $c$-axis as indeed is observed [7].

Within this theoretical framework, magnetic R-ions may appear to play only a spectator role with respect to the ferroelectric properties of the $RMnO_3$ manganites. However more recently we have understood from both theoretical and experimental work that they can strongly influence multiferroic properties [16, 19, 20]. Their role needs to be taken into account in order to arrive at a quantitative model for the ferroelectric polarization, and to understand the behavior of the magnetic structure under an applied magnetic field [17]. Indeed from phenomenology, the magnetic anisotropy provided from R-spins appears to be one of the critical parameters that results in the flop of the Mn cycloid with magnetic field and therefore the flop of $\mathbf{P}_s$ from the $c$- to the $a$-axis [17].

In this paper we discuss the details of the magnetic ordering in the R = Tb and Dy multiferroic manganites and focus on the nature of the ordering of R-spins and its relevance to multiferroic behavior. In section 2 we describe

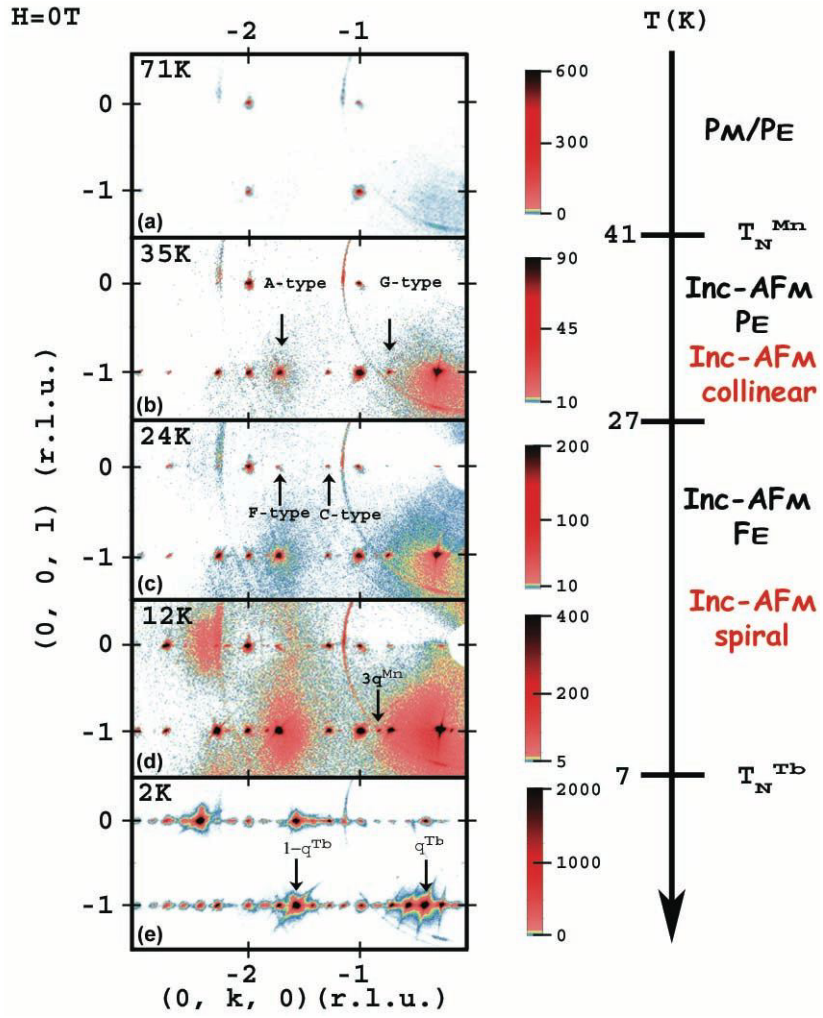


**Figure 2.** Cuts of reciprocal space measured from a $TbMnO_3$ single crystal in the (1, 0, 0) plane at various temperatures, using the E2 flat cone diffractometer at the Hahn-Meitner-Institute's BENSC facility. Here we used an incident wavelength $\lambda = 2.3962$ Å from a PG002 monochromator. Graphite and Ge filters were used in the primary beam to suppress $\lambda/2$ and $\lambda/3$ contamination, respectively. Incommensurate magnetic reflections are labeled in terms of the four expected modes. Intensity scales for each temperature are shown on the right side of each panel. The progression of the various phase transitions in temperature is also shown as paramagnetic/paraelectric (PM/PE), incommensurate antiferromagnetic (Inc-AFM) and ferroelectric (FE).

measurements on $TbMnO_3$ using single crystal unpolarized and polarized neutron diffraction as a function of temperature and magnetic field. These measurements reveal not only the direction of the various components of the magnetization but also provide information as to which magnetic species (Mn or Tb) contributes to them. In section 3 we describe x-ray resonant magnetic scattering (XRMS) measurements which demonstrate that the Mn–R magnetic interaction ($J_{Mn-R}$) is a significant parameter when considering the magnetic ordering of these multiferroics. We describe a frustrated ANNNI model coupled to a periodic external field produced by the Mn-spin order which describes the magnetic ordering of Tb, Dy and Ho in the $RMnO_3$ manganite perovskites. Finally in section 4 we show how Dy-spins play an active role enhancing the ferroelectric polarization in $DyMnO_3$. We offer a theoretical argument of how the coupling of R-spins to the Mn cycloid can enhance the ferroelectric polarization and on this basis we use neutron diffraction measurements to quantitatively account for the enhanced polarization.

## 2. Magnetic ordering in $TbMnO_3$

The magnetic structure of multiferroic $RMnO_3$ is complex not only because of the cycloidal ordering of Mn-spins but also due to the ordering of R-spins. This complexity is clearly seen in neutron diffraction measurements where a number of incommensurate reflections are observed as a function of temperature [21]. Using the flat cone neutron diffractometer E2 at the Hahn-Meitner-Institut's BENSC facility, we carried out a temperature dependent survey of reciprocal space in the (100) plane of $TbMnO_3$ (figure 2). In agreement with previous measurements we find incommensurate magnetic reflections appearing in different Brillouin zones (BZ) as the sample is cooled from 71 to 2 K [10, 15, 21]. From Bertaut's representational theory the magnetic ordering of Mn-spins with space group $Pbnm$ and $\tau^{Mn} = 0.27\mathbf{b}^*$ can be described by four irreducible representations ($\Gamma$) that consist of four modes (labeled as A, C, F and G) [22, 23]. The modes correspond to magnetic superlattice reflections that occur in

different Brillouin zones with extinction conditions as follows; $A$ for $h+k=$ even, $l=$ odd; $G$ for $h+k=$ odd with $l=$ odd; $F$ for $h+k=$ even and $l=$ even; and $C$ for $h+k=$ odd and $l=$ even, where $h, k, l$ are Miller indices. Each mode here describes the Mn-spin polarization along one unique principle crystallographic axis [22, 23].

On cooling below $T_N$ we observe reflections that belong to the A- and G-modes as shown in figure 2(b), while below $T_S$ we observe reflections from the F- and C-modes (figure 2(c)). The intensity of the A-mode reflections rapidly increases on cooling (see figure 4(a)) and show an anomaly below $T_S$, indicative of the development of a $c$-axis component as the Mn ordering evolves from a SDW to a cycloid [14]. The C-, F- and G-modes have a significantly different temperature dependence in that their intensity on cooling exhibits a concave-up curvature [14] (see figures 4(b)–(d)) that is interpreted to arise from the induced ordering of Tb-spins. On cooling further below $T_N^{Tb}$ we find new satellite reflections that are assigned to the independent ordering of Tb-spins with propagation vector $\tau^{Tb} \sim 0.42\mathbf{b}^*$ (figure 2(e)). The assignment of these reflections to Tb-spin-ordering is made on the basis of specific heat data which show a large peak at 7 K [7]. More recently this assignment has been confirmed with XRMS [19, 24] and will be discussed in the following section. The data in figure 2 also show diffuse scattering below $T_N$ in positions close to $\tau^{Tb} \sim 0.42\mathbf{b}^*$. This suggests that—at least as high as 35 K—short range correlations of Tb-spins are present.

The SDW phase above $T_S$ can be described by a single irreducible representation $\Gamma_3 = (G_x, A_y, F_z)$ using the notation of Brinks *et al* [23] where subscripts indicate that the magnetic polarization of each mode. For the SDW phase at 35 K Kenzelmann *et al* [15] compute a value of $\mathbf{m}^{Mn} = (0.0(0), 2.90(5), 0.0(0))\ \mu_B$/Mn indicating that only the $A_y$ mode is active. Below $T_S$, in the cycloidal phase, the ordering of Mn-spins is described by the coupling of two irreducible representations, $\Gamma_2 \times \Gamma_3$ [23], where $\Gamma_2 = (C_x, F_y, A_z)$ [23]. The Mn-spins rotate within the $bc$-plane and their ordering is described by two A-modes, $A_y, A_z$ [15, 23]. Indeed Kenzelmann *et al* [15], using unpolarized neutron diffraction measurements, find values for these two components of 3.9(1) and 2.8(1) $\mu_B$/Mn respectively [15], demonstrating that the cycloid is elliptical, with a phase difference between the $A_y$ and $A_z$ modes fixed to $\pi/2$ [15].

What is puzzling with the temperature dependent measurements of these magnetic reflections is that the intensity of the C, F and G-modes, which presumably arise from induced Tb ordering, do not decrease below $T_N^{Tb}$. Indeed in $DyMnO_3$ the independent ordering of Dy-spins leads to a decrease in the intensity of reflections with wavevector $\tau^{Mn}$ (see section 4) [16, 20]. As we shall see in sections 2.2 and 3.1 this behavior arises from a harmonic matching of the $\tau^{Tb}$ and $\tau^{Mn}$ wavevectors below $T_N^{Tb}$. Above $T_N^{Tb}$ evidence for an induced ordering of Tb-spins with $\tau^{Tb} = \tau^{Mn}$ was reported by Kenzelmann *et al* as they find a best fit of their data to a model of the magnetic structure of $TbMnO_3$ where Tb-spins are ordered at 12 K along the $a$-axis [15].

### 2.1. Field dependence of magnetic reflections

The picture that emerges from the diffraction data is that both Tb- and Mn-spin-ordering can indeed contribute to the intensities of magnetic reflections. We have found that tracking the intensity of these reflections in an applied magnetic field can allow one to assign these reflections to Mn-or Tb-spin order or both in the temperature region between $T_N^{Tb} < T < T_N$. Below we briefly describe the field dependence of $\tau^{Mn}$ and $\tau^{Tb}$ reflections measured with unpolarized neutrons with a magnetic field up to 14 T applied along the $a$-axis ($H \parallel a$).

We first turn our attention to the field dependence of the Tb-spin-ordering below $T_N^{Tb}$. In figure 3 we show the field dependence of the $(0, \tau^{Tb}, 1)$, (0, 0, 2), (0, 1, 1) and (0, 2, 0) reflections at various temperatures. At 2 and 5 K the application of a 2 T field completely suppresses the intensity of the $(0, \tau^{Tb}, 1)$ reflection (figure 3(a)), while at the same time we find a large increase in the integrated intensity of the (0, 2, 0), (0, 0, 2) and (0, 1, 1) reflections (figures 3(c) and (d)). These data suggest that for $T < T_N^{Tb}$ an application of a relatively small field, $H \parallel a = 2$ T, polarizes the Tb-spins ferromagnetically. This behavior is also reflected in magnetization data for the same geometry where a spontaneous magnetization is found to develop with an applied magnetic field along the $a$-axis [6]. For $T > T_N^{Tb}$ we also find an increase in the intensity of commensurate Bragg reflections, but this increase is less abrupt compared to $T < T_N^{Tb}$, suggesting that larger fields are needed to polarize Tb-spins. We believe that the ferromagnetic signal we find here for $T > T_N^{Tb}$ is unlikely to arise from the alignment of Mn-spins, as this would completely destroy the ferroelectric polarization, contrary to observations [6].

In figure 4 we show the temperature dependence of reflections representing the four modes in various fields applied parallel to the $a$-axis ($H \parallel a$). For the C-, F- and G-modes (see figures 4(b) and (c)) we find that down to 7 K their intensity increases on cooling in a 2 T field, similar to the zero field cooled (ZFC) measurements down to $T_N^{Tb}$. However, for all three modes we find a sharp decrease of their intensity below $T_N^{Tb}$, in contrast to the zero field data. This decrease is coupled to the increase of ferromagnetic scattering as shown in figure 3, confirming that Tb-spins contribute to the intensity of the C-, F- and G-modes. For field cooled measurements at higher field, we find a large suppression of the intensity of these reflections compared to the zero field data and an absence of anomalies in the proximity of $T_N^{Tb}$, again in agreement with the data shown in figure 3. In contrast to the other reflections the intensity of the A-mode is enhanced under magnetic field and possibly reflects changes in the Mn-spin arrangement.

### 2.2. Polarized neutron diffraction investigation of $TbMnO_3$

While in the previous sections we have established that the Mn ordering is essentially described by the A-mode, and the C-, F- and G-modes describe the induced Tb ordering, it still remains to determine the polarization of these modes and compare them with the proposed model of the magnetic structure. To establish the polarization of the four modes we have employed the XYZ polarized neutron diffraction method [25, 26]. This

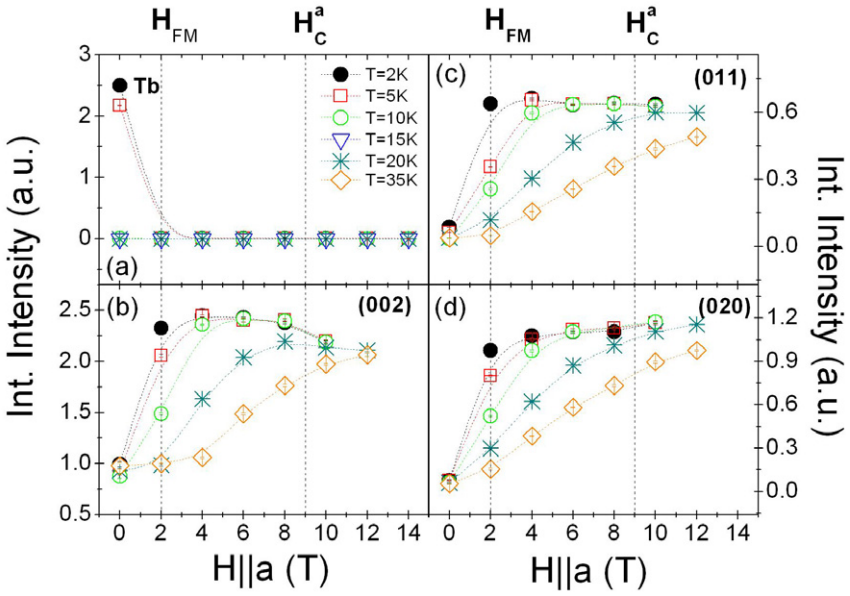


**Figure 3.** Temperature dependence of integrated intensity for the (a) (0, $\tau^{\mathrm{Tb}}$, 1), (b) (002), (c) (011) and (d) (020) reflections measured in various magnetic fields applied along the $a$-axis. The integrated intensity of all reflections has been normalized to the A-mode reflection taken at $H = 0$ T and $T = 2$ K (see figure 4).

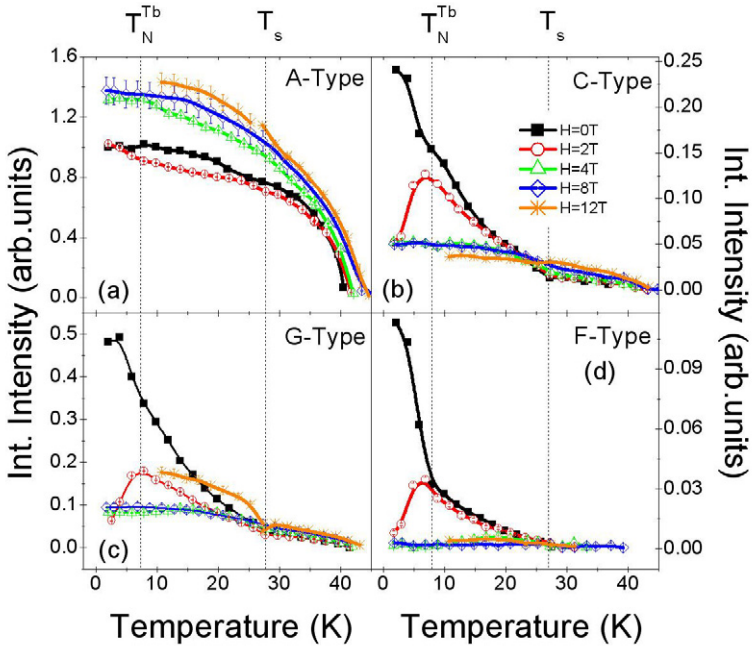


**Figure 4.** Temperature dependence of integrated intensity for the (a) A (0, $\tau^{\mathrm{Mn}}$, 1), (b) C (0, $1 + \tau^{\mathrm{Mn}}$, 2), (c) F (0, $\tau^{\mathrm{Mn}}$, 2) and (d) G (0, $1 - \tau^{\mathrm{Mn}}$, 1) mode reflections cooled in various magnetic fields applied along the $a$-axis. Intensities have been normalized to the A-mode at 2 K and $H = 0$ T.

method uses neutron polarization analysis to determine the spin flip ($I^{\uparrow\downarrow}$) and non-spin flip ($I^{\uparrow\uparrow}$) intensity of each magnetic reflection. The direction of the neutron's spin is controlled by three Helmholtz coils that surround the sample, allowing us to align it either parallel to the scattering vector $\mathbf{Q}$ ($x$-channel) or along the two perpendicular directions within the scattering plane ($y$-channel) or perpendicular to it ($z$-channel). In total, six measurements are made for each reflection and results are corrected for the Lorentz factor, absorption and polarization efficiency. In this geometry the scattering plane is horizontal and parallel to the coils $xy$-plane, while $z$- is vertical to the scattering plane.

In our experiment a $TbMnO_3$ single crystal was oriented to probe magnetic reflections in the $bc$-plane at 12 K while $I^{\uparrow\downarrow}$ and $I^{\uparrow\uparrow}$ measurements of all modes were measured along the three channels. From these data we compute the flipping ratio

**Table 1.** Normalized spin flip ($I^{\uparrow\downarrow}$) and non-spin flip ($I^{\uparrow\uparrow}$) intensity ratios of the A, C, F and G reflections measured at $T = 12.5$ K are used to compute the flipping $R = (I^{\uparrow\uparrow} - I^{\uparrow\downarrow})/(I^{\uparrow\uparrow} + I^{\uparrow\downarrow})$. The integrated intensity of each cross-section ($I$) is corrected for absorption and extinction. Below we tabulate $R$ for various reflections in two scattering geometries; $a$-axis is placed vertical and A, C, F and G reflections are measured and $c$-axis is placed vertical and only F and C reflections are measured. The subscript in $R$ indicates the polarization of the neutron with respect to the orientation of the Helmholtz coils. The intensity ratio between ($\uparrow\downarrow$) and ($\downarrow\uparrow$) flipper configuration were found to be unchanged. $\alpha$ indicates the angle between **Q** and the $b$-axis. The total intensity of each reflection is given as $I^{\uparrow\downarrow} + I^{\uparrow\uparrow}$ summed over the three channels. These measurements were taken using the V2 spectrometer at the Hahn-Meitner-Institute's BENSC facility. Here we used $k_i = 1.5$ Å$^{-1}$, while a cooled Be filter was used to suppress $\lambda/2$ contamination. Neutron polarization was achieved with polarized cavities positioned after the Be filter. The sample was inserted within an $XYZ$ Helmholtz coils. Two Mezei flipper coils were placed just before and after the sample.

| $(h, k, l)$ | $\alpha$ | $R_{\|x}$ | $R_{\|y}$ | $R_{\|z}$ | $I^{\uparrow\uparrow} + I^{\uparrow\downarrow}$ |
|---|---|---|---|---|---|
| | | $z \parallel a$ configuration | | | |
| | | A-mode | | | |
| (0, 2.272, 1) | 19.1 | −0.90(3) | 0.84(3) | −0.94(3) | 3333 |
| (0, 1.728, 1) | 24.6 | −0.94(2) | 0.96(2) | −0.94(2) | 3333 |
| (0, 0.272, 1) | 70.9 | −0.96(2) | 0.96(2) | −0.98(1) | 4795 |
| (0, 0.272, 3) | 83.5 | −0.94(3) | 0.90(3) | −0.98(3) | 4640 |
| | | C-mode | | | |
| (0, 0.728, 0) | 0.0 | −1.00(4) | −1.00(4) | 1.00(4) | 35 |
| (0, 1.272, 0) | 0.0 | −0.96(3) | −0.90(5) | 0.90(2) | 1644 |
| (0, 1.272, 2) | 61.1 | −0.76(3) | −0.94(3) | 0.68(3) | 160 |
| (0, 0.728, 2) | 75.2 | −1.00(3) | −1.00(3) | 1.00(3) | 30 |
| | | F-mode | | | |
| (0, 1.728, 0) | 0.0 | −0.96(2) | 0.86(2) | −0.92(2) | 54 |
| (0, 2.272, 0) | 0.0 | −0.90(5) | 0.90(8) | −0.90(5) | 65 |
| (0, 1.728, 2) | 53.7 | −0.86(3) | 0.80(5) | −0.86(3) | 43 |
| (0, 0.272, 2) | 80.2 | −1.00(3) | 0.94(3) | −0.98(3) | 24 |
| | | G-mode | | | |
| (0, 1.272, 1) | 31.8 | −0.88(2) | −0.96(2) | 0.84(2) | 551 |
| (0, 0.728, 1) | 47.5 | −0.76(2) | −0.76(2) | 0.72(2) | 682 |
| (0, 0.728, 3) | 73.0 | −0.94(2) | −0.94(2) | 0.92(2) | 885 |
| | | $z \parallel c$ configuration | | | |
| | | C-mode | | | |
| (1, 2.272, 0) | 25.8 | −0.90(5) | 0.90(5) | −0.98(5) | 200 |
| (1, 0.272, 0) | 76.1 | −0.96(4) | 0.90(5) | −0.96(4) | 382 |
| | | F-mode | | | |
| (1, 0.728, 0) | 56.5 | −0.98(5) | −0.64(5) | 0.56(5) | 325 |

$R = (I^{\uparrow\downarrow} - I^{\uparrow\uparrow})/(I^{\uparrow\downarrow} + I^{\uparrow\uparrow})$ for each channel. Data were collected as a function of $\alpha$, the angle between the scattering vector **Q** and the $b$-axis. In our geometry for a value of $R = 1$ for $\alpha = 0$ in the $y$-channel indicates that spins are polarized along the $c$-axis (**Q** $\parallel$ $b$ and $y$-channel $\parallel$ $c$). Data were also measured for the C- and F-modes with the crystal mounted with the $ab$-plane in the horizontal plane. The results of these measurements are given in table 1.

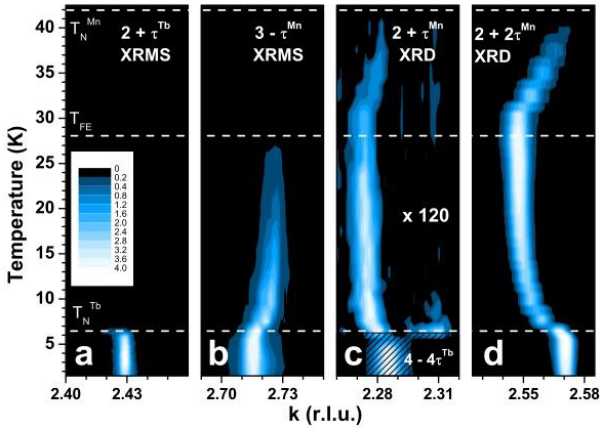


**Figure 5.** Temperature dependence of characteristic magnetic and lattice distortion reflections in the form of an intensity plot measured using XRMS and XRD. In panels (a) and (b) we show $\sigma$–$\pi'$ data measured from the $\tau^{\mathrm{Tb}}$ and $\tau^{\mathrm{Mn}}$ peak in the (0 $k$ 2) zone with the x-ray energy tuned to the Tb $L_2$ edge. In panels (c) and (d) we shown XRD data of the $\tau^{\mathrm{Mn}}$ and $2\tau^{\mathrm{Mn}}$ reflections measured in the (0 $k$ 3) and (0 $k$ 2) Brillouin zones, respectively. The $\tau^{\mathrm{Mn}}$ reflections in panel (c) is $2 \times 10^{-9}$ smaller in intensity than the neighboring (023) reflection and represent only magnetic scattering. Below $T_{\mathrm{N}}^{\mathrm{Tb}}$ the weak (0, $2 + \tau^{\mathrm{Mn}}$, 3) reflection is superposed by a 100 times stronger reflection from a structural distortion, $-4\tau^{\mathrm{Tb}}$, related to the Tb ordering. The intensity scale in panel (c) is broken close to $T_{\mathrm{N}}^{\mathrm{Tb}}$ and a linear background has been subtracted. The $2\tau^{\mathrm{Mn}}$ in panel (d) is the expected second harmonic structural reflection.

The A-mode is in principle polarized both along the $b$- and $c$-direction as illustrated in figure 5(b) [15]. In this experiment we can only test for the $b$-axis component which we find to be in agreement with flipping ratios of $R_y \sim 1$ for A-mode reflections shown in table 1. To test for the $c$-axis component (and thus for the cycloid) one would need a crystal orientation in which $h \neq 0$ within the scattering plane, a condition that was impossible to satisfy within our experimental geometry. For the G-mode we find clear evidence from table 1 that it is polarized along the $a$-axis. A small component perpendicular to the $a$-axis indicated by the (0, 0.728, 1) reflection is not significant as the intensity of this reflection is small. Finally for the C- and F-modes with $h = l = 0$, the scattering vector is parallel to the $b$-axis (**Q** $\parallel$ $b$, $\alpha = 0$) and it is straightforward to deduce that the these two modes represent components of the magnetization parallel to the $a$- and $c$-axis, respectively. This is also confirmed by changing the alignment of the crystal with respect to the coil directions and probing the C- and F-modes with the $c$-axis vertical.

### *2.3. The magnetic structure of $TbMnO_3$*

The polarized and unpolarized neutron diffraction measurements show a complex behavior for the various magnetic reflections of $TbMnO_3$ as function of field and temperature. The behavior of the A-mode reflections both in terms of temperature, field and neutron polarization are compatible with the $bc$-cycloid model of Kenzelmann *et al* [15]. The C- and F-mode can be reliably assigned to Tb-spin order that is clamped to the Mn magnetic ordering for $T_{\mathrm{N}}^{\mathrm{Tb}} < T < T_{\mathrm{N}}$. Our measure-

ments indicate that Tb-spins not only have an $a$-axis component as suggested previously [15], but also a $c$-axis component (F- mode). The size of this $c$-axis component should be less than 1 $\mu_B$/Tb by comparison to the intensities of C-mode reflections (see table 1). The case of the G-mode is less straightforward. This mode appears below $T_N$ and has a concave-up temperature dependence similar to the F- and C-modes as well as a decrease in its intensity at $T_N^{Tb}$ under applied field. This would indicate at first sight that it could arise from induced Tb ordering. However, in the SDW phase the $\Gamma_3$ representation allows Tb-spins to order only along the $c$-axis while a $G_x$ mode is allowed only for Mn-spins [23]. Below $T_S$, the coupled $\Gamma_3 \times \Gamma_2$ does allow for Tb-spins to also have components along all three crystallographic axis. The observation of both C- and G-modes polarized along the $a$-axis is possible given the specific symmetry of the Tb site [22, 23]. So in conclusion the G-mode can reflect contributions of both Tb- and Mn-spins below $T_S$ but only contribution by Mn-spins are allowed by symmetry in the temperature range $T_S < T < T_N$. From these data it is not clear how large the contribution of the Tb-spins is to the intensity of the G-mode below $T_S$. The phase relationship between the C-, F- and G-modes was not established.

The conclusions that we can draw from these measurements on the magnetic ordering of $TbMnO_3$ in the ferroelectric phase at 12 K are; (i) the magnetic scattering of Mn-spins is contained in the A-mode and to a lesser extent in the G-mode which represents a polarization of the Mn-spin along the $a$-axis. (ii) The ordering of Tb-spins gives rise to C-, F- and G-modes where the first two are polarized along the $a$-, $c$-axis respectively. This demonstrates that the induced ordering of Tb-spins is more complex than proposed previously.

## 3. Coupling of R- and Mn-spins in multiferroic $RMnO_3$

The induced ordering of R-spins due to Mn-spin-ordering naturally leads to a clamping of their wavevectors below $T_N$. This behavior was first noted in R = Ho, where the analysis of neutron diffraction data assuming a pure $Mn^{3+}$ ordering led to nonrealistic values of the Mn magnetic moment [23]. It was found that Ho-spins are always clamped to Mn-spins even as $\tau^{Mn}$ is incommensurate above 26 K, and locks in to a value of $\tau^{Mn} = (1/2)\mathbf{b}^*$ below [13]. The ferroelectric properties of this compound were unknown at that time but a recent report suggests that an induced moment on Ho only exists in the ferroelectric phase of this compound [27]. For R = Dy a similar behavior is found in XRMS measurements with a low temperature commensurate ordering of Dy-spins with $\tau^{\mathbf{Dy}} = (1/2)\mathbf{b}^*$ ($\tau^{\mathbf{Mn}} \approx 0.38\mathbf{b}^*$) [16]. For R = Tb, we do not find a commensurate order as in the two previous examples. Instead we find a clamping of both Tb- and Mn-spins even below $T_N^{Tb}$. Finally, for R = Gd, preliminary XRMS data show that the Gd-spin-ordering wavevector is $\tau^{\mathbf{Gd}} = (1/4)\mathbf{b}^*$ [28], while for the Mn ordering $\tau^{\mathbf{Mn}} = 0$ has been reported below 24 K from non-resonant XRD studies [29].

It is interesting to compare this behavior with the isostructural orthoaluminates $RAlO_3$ with R = Tb, Dy and Ho. All three compounds have relatively low ordering temperatures with $T_N^R$ in the order of 3 K [30]. They show the same type of commensurate $\tau = 0$ antiferromagnetic ground state, where R-spins are confined within the $ab$ plane and their magnetic structure can be represented as ($G_x$, $A_y$, 0) in Bertaut notation [30]. In this case, the Dy- and Tb-ions can be treated as Ising ions, with their anisotropy axis lying in the $ab$ plane. In the manganites, where the magnetic structure is commensurate for Dy and Ho, the R moments still keep the same ($G_x$ $A_y$ 0) coupling while the magnetic unit cell is doubled along the $b$-direction. These comparisons demonstrate the $J_{R-R}$ is about an order of magnitude smaller than $J_{Mn-Mn}$ and that R-spins maintain the general features of their magnetic ordering even in the presence of a magnetic B site cation such as Mn.

### 3.1. Long range ordering of the R moments

Induced R ordering in the ferroelectric state of multiferroic manganites has been observed directly using XRMS [19, 20, 24, 31]. The specific feature of XRMS is its element selectivity using resonances allowing one to assign the observed feature to the corresponding chemical element. In figure 5 we show color contour plots of the temperature dependence of XRMS measurements at the Tb $L_2$ edge for $\tau^{Tb}$ and $\tau^{Mn}$ reflections as well as non-resonant x-ray diffraction (XRD) measurements of the $\tau^{Mn}$ and $2\tau^{Mn}$ reflections in $TbMnO_3$. Figures 5(a) and (b) show of the temperature dependences of selected Bragg reflections with the x-ray energy tuned to the Tb $L_2$ edge, providing sensitivity to the Tb contribution. Below $T_S$, a number of resonant $(0, k \pm \tau^{Mn}, l)$ reflections are detected in the $\sigma$–$\pi'$ polarization channel. This shows that Tb orders magnetically with the same wavevector as Mn, $\tau_1^{Tb} = \tau^{Mn} = 0.274(1)$ at 27 K. These reflections are observed below $T_S$ and their intensity increases with concave curvature on cooling—as noted in the previous section. Below $T_N^{Tb}$ this effect is accompanied by the appearance of much stronger $(0, k \pm \tau_2^{Tb}, l)$ reflections corresponding to a separate ordering of Tb with an incommensurate propagation vector $\tau_2^{Tb} = 0.4285(10)$ [19].

While the coupling between Mn- and Tb-spins for $T > T_N^{Tb}$ was described above, below $T_N^{Tb}$ we find a significant shift of $\tau^{Mn}$ from a value of ~0.274 to 0.286(1). This effect is shown in figures 5(c) and (d) where we show temperature dependent measurements of the non-resonant A-type reflection $(0, 2 + \tau^{Mn}, 3)$ (which has only $2 \times 10^{-9}$ the intensity of the neighboring (0 2 3) reflection) and the second harmonic reflection $(0, 2 + 2\tau^{Mn}, 2)$, representing directly the Mn magnetic ordering and the accompanied lattice distortion, respectively. Below $T_N^{Tb}$, both peaks shift simultaneously showing that indeed $\tau^{Tb}$ shifts from $0.274\mathbf{b}^*$ at $T_N^{Tb}$ to $0.286\mathbf{b}^*$ just below it. The temperature dependence of the $\tau^{Mn}$ peak intensities in (b) is surprising as it even increases across the transition below $T_N^{Tb}$. One would expect that if Tb-spins order independently below this temperature that in neutron or x-ray measurements the intensity of the $\tau^{Mn}$ peak, characterizing the Tb-spin polarization with the Mn wavevector, would decrease below $T_N^{Tb}$. This apparent contradiction is understood better by noting that below $T_N^{Tb}$ the values of $\tau^{Mn}$ and $\tau^{Tb}$ are closely related. We find that with this ordering of Mn- and Tb-spins the relationship $3\tau^{Tb} - \tau^{Mn} = 1$ holds to an accuracy

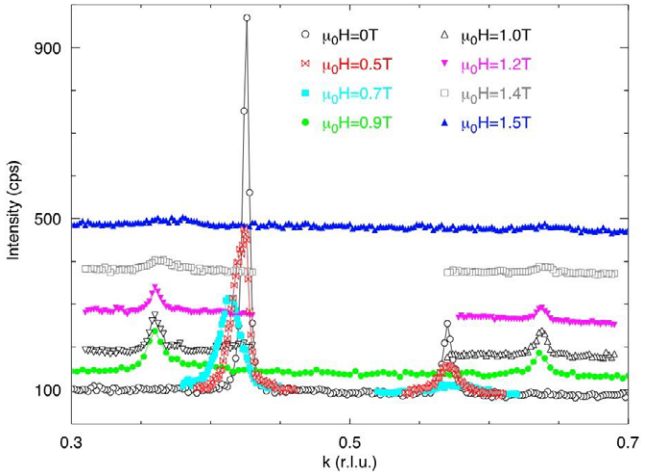


**Figure 6.** Scans along $k$-direction of the $(0, \tau^{\mathrm{Tb}}, 5)$ and $(0, 1-\tau^{\mathrm{Tb}}, 5)$ reflection on Tb $L_2$-resonance as function of field $H \parallel a$ at a sample temperature $T = 4$ K. The measurements were conducted with an analyzer to reduce background (PG(002)). Polarization analysis (PG(006)) revealed all the intensity in the $\pi$–$\pi'$ channel in accordance with the Tb-moment oriented along the $a$-direction. These measurements were taken using beamline X21 at the National Synchrotron Light Source (NSLS) at Brookhaven National Laboratory. A 13 T vertical field superconducting magnet was used to apply a magnetic field parallel to the $a$-axis.

of $10^{-4}$ [19], i.e., the third harmonic of the Tb wavevector matches that of the Mn order. Indeed the ground state values of $\tau^{\mathrm{Mn}}$ and $\tau^{\mathrm{Tb}}$ are very close to the rational fractions 2/7 and 3/7, respectively [19]. The implication of these measurements is that there is no real independent ordering of Tb-spins below $T_{\mathrm{N}}^{\mathrm{Tb}}$ as might have been expected from the behavior of the R = Dy and Ho manganites. The coupling of Tb- and Mn-spins that we find above $T_{\mathrm{N}}^{\mathrm{Tb}}$ also persists below, but takes on a different form.

### 3.2. High field measurements

The $3\tau^{\mathrm{Tb}} - \tau^{\mathrm{Mn}} = 1$ wavevector relationship can be modulated by applying a magnetic field along the $a$-axis ($H \parallel a$). In figure 6 we show measurements of the $(0, \tau^{\mathrm{Tb}}, 5)$ and $(0, 1-\tau^{\mathrm{Tb}}, 5)$ reflections measured at the Tb $L_2$ resonance as function of magnetic field. When we apply a magnetic field parallel to the $a$-axis we find that the intensity of these reflections decreases significantly with relatively small fields of up to 0.7 T. At 0.9 T these reflections have essentially disappeared and we find new reflections with $\tau = 0.361(1)\mathbf{b}^*$ instead. We find a similar behavior for the $\tau^{\mathrm{Mn}}$ reflection in that they show a discontinuous transition from $\tau^{\mathrm{Mn}} = 0.285(1)\mathbf{b}^*$ down to $0.276(1)\mathbf{b}^*$ (not shown). In this geometry, due to the alignment of the induced Tb magnetic moment along the $a$-axis [15], for $(0, \tau^{\mathrm{Tb}}, 5)$ and $(0, 1-\tau^{\mathrm{Tb}}, 5)$ we only find intensity in the $\pi$–$\pi'$ channel, in agreement with the resonant magnetic scattering cross-section. The transition found here changes the wavevectors of both the Mn- and Tb-spin-ordering discontinuously and is reminiscent of the transition at $T_{\mathrm{N}}^{\mathrm{Tb}}$ in zero field. The actual values of the $\tau^{\mathrm{Tb}}$ and $\tau^{\mathrm{Mn}}$ wavevectors in this new in-field regime are close to the rational fractions of 4/11 and 3/11 respectively, while the wavevectors hold the relationship of $2\tau^{\mathrm{Tb}} + \tau^{\mathrm{Mn}} = 1$ within 0.005 accuracy. Increasing the applied field above $H \parallel a = 1.4$ T leads to a melting of this coupled ordering as Tb-spins align ferromagnetically as discussed earlier [32]. Our measurements of neutron and x-ray diffraction with magnetic fields applied parallel to the $b$-axis do not show similar effects as found here for $H \parallel a$. Rather, for $H \parallel b$ we find a transition to $\tau^{\mathrm{Tb}} = (1/3)\mathbf{b}^*$ at 1.2 and at 5 T a transition associated with the polarization flop which drives $\tau^{\mathrm{Mn}}$ to the commensurate value of $(1/4)\mathbf{b}^*$ [32].

### 3.3. Coupling of Ising R-spins to the Mn cycloid

From the measurements we have described so far for R = Tb, the picture that emerges is one in which R-spins attempt to find the best possible ordering within a background of a Mn cycloid. To gain further insight into this problem one can treat this situation phenomenologically where we consider the ordering of one SDW in a magnetic background given by another SDW (in this case that from Mn-spins). In zero field we find a quartic coupling $gL_{\mathrm{Tb}}^3 L_{\mathrm{Mn}}$ between the Tb and Mn magnetic order parameters, which favors a relation of the type $3\tau^{\mathrm{Tb}} \pm \tau^{\mathrm{Mn}} = n$ ($n$ is an integer number) between the wavevectors of the two spin-density waves. This is consistent with the observed relation $3\tau^{\mathrm{Tb}} - \tau^{\mathrm{Mn}} = 1$ found for R = Tb in zero field. In an applied magnetic field, the Tb SDW acquires a homogeneous component $\chi H$ and the quartic term effectively leads to the coupling $3g\chi H L_{\mathrm{Tb}}^2 L_{\mathrm{Mn}}$ favoring $2\tau^{\mathrm{Tb}} \pm \tau^{\mathrm{Mn}} = n$, that explains the switch in the relation between the Tb- and Mn-spins observed for $H \parallel a$.

While the phenomenological approach is valid close to $T_{\mathrm{N}}^{\mathrm{Tb}}$, at zero temperature Tb-spins can be considered as Ising-like [33, 34] and cannot be described by a small number of Fourier harmonics. To understand the interplay between the R and Mn orderings we consider a one-dimensional ANNNI Ising model,

$$E = \sum_y \left[ J\sigma_y\sigma_{y+1/2} + J'\sigma_y\sigma_{y+1} - \lambda\sigma_y \cos(Qy + \phi) \right], \tag{1}$$

where the Ising variables $\sigma_y = \pm 1$ describe R-spins at the sites $y = 0, 1/2, 1, 3/2, 2, \ldots$, coupled to the periodically varying 'external field' induced by Mn-spins, so that $Q = \tau^{\mathrm{Mn}} = 2/7$ and $\lambda \propto J_{\mathrm{Mn-Tb}}$. The unit cell of the chain contains two spins (one with an integer and one with an half-integer coordinate) corresponding to two R-ions in each $ab$-layer of the unit cell of $RMnO_3$. For ferromagnetic nearest-neighbor coupling, $J < 0$, antiferromagnetic next-nearest-coupling, $J' > 0$, and $\lambda = 0$ we recover the usual ANNNI model, which has the FM ground state ($\tau^{\mathrm{Tb}} = 0$) for $\kappa = \frac{J'}{|J|} < \frac{1}{2}$ and the $\uparrow\uparrow\downarrow\downarrow$-state ($\tau^{\mathrm{Tb}} = 1/2$), for $\kappa > \frac{1}{2}$.

We now compare energies of the states with $\tau^{\mathrm{Tb}} = 2/7$, 3/7 and 1/2 corresponding to, respectively, 4, 6, and 7 domain walls in the interval of 7 unit cells (14 spins). For $\kappa > 1/2$ the domain wall energy is negative and the $\uparrow\uparrow\downarrow\downarrow$-state with the highest number of DWs has the lowest energy, if only interactions between Tb-spins are considered. The energy of the Tb–Mn interaction in $\uparrow\uparrow\downarrow\downarrow$-state is zero, while for

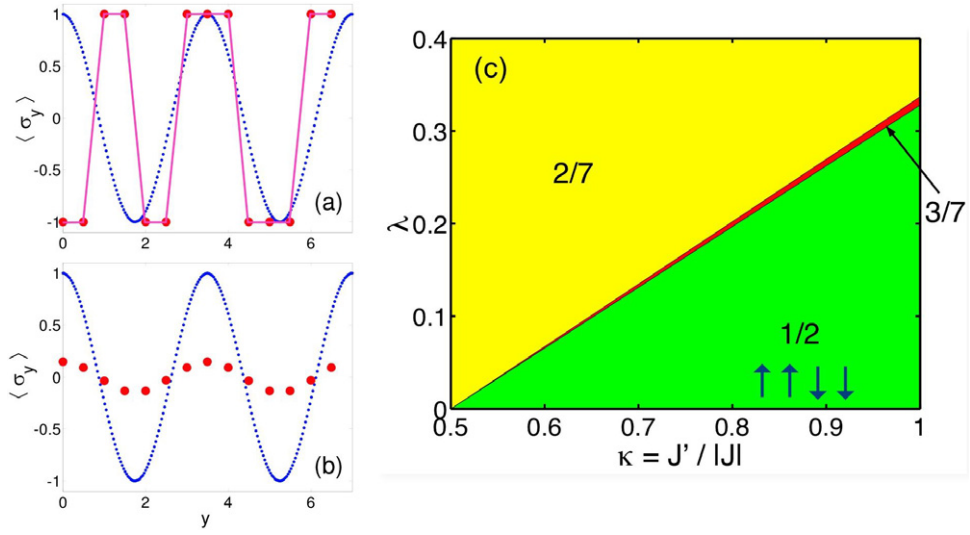


**Figure 7.** Average values of R-spins (red circles) described by the frustrated Ising model in a periodically varying external field (dotted blue line) at zero temperature (a) and at high temperatures (b). In the latter case $\tau^{\mathrm{Tb}} = \tau^{\mathrm{Mn}} = 2/7$, while at $T = 0$, $\tau^{\mathrm{Tb}} = 3/7$. (c) Zero temperature phase diagram of model (1). The phases are numbered by the wavevector $\tau^{\mathrm{Tb}}$ of the main spin modulation: $\tau^{\mathrm{Tb}} = 2/7$ (light), $\tau^{\mathrm{Tb}} = 3/7$ (dark), $\tau^{\mathrm{Tb}} = 1/2$ (darker).

the state with $\tau^{\mathrm{Tb}} = \tau^{\mathrm{Mn}} = 2/7$ it is $-0.642\lambda$ per spin. Surprisingly, the state with $\tau^{\mathrm{Tb}} = 3/7$ also gains a substantial energy due to the interaction with Mn-spins, which for the best possible arrangement of 6 domain walls, shown in figure 7(a), is $-0.218\lambda$ per spin.

The resulting zero temperature phase diagram is shown in figure 7(c). For the weak R–Mn coupling regime, the ↑↑↓↓-state has the lowest energy and the wavevectors of R and Mn orderings are decoupled as is the case for R = Dy [16]. For large $\lambda$, $\tau^{\mathrm{R}} = \tau^{\mathrm{Mn}}$ down to zero temperature as found for R = Ho [13, 23]. In the narrow sector $0.656 < \frac{\lambda}{2J'+J} < 0.674$, Ising spins order in the ground state with $\tau^{\mathrm{Tb}} = 3/7$, as observed in $TbMnO_3$. This is a rather unexpected result since the 3/7-state is stabilized by the modulation of Mn-spins with a different wavevector. Numerical mean field studies of the three-dimensional version of model (1) for parameters favoring the 3/7-state show that at high temperatures the wavevector of the Tb modulation equals that of Mn-spins (see figure 7(b)), while below $T_{\mathrm{N}}^{\mathrm{Tb}}$ the intensity of the $\tau^{\mathrm{Tb}} = 3/7$ peak is several times higher than that of the $\tau^{\mathrm{Tb}} = 2/7$ peak, in agreement with our diffraction data. The small extent of the 3/7-region in the phase diagram of our model suggests that other mechanisms, e.g. longer range interactions between R-spins and the deformation of the Mn SDW in response to the ordering Tb-spins, may contribute to a stabilization of this phase.

These results on $TbMnO_3$ show that the $J_{\mathrm{Mn-R}}$ interaction is a critical ingredient in our understanding of the magnetism and physical properties of multiferroic manganites with magnetic R-ions. In the temperature range $T_{\mathrm{N}}^{\mathrm{R}} < T < T_{\mathrm{S}}$ the coupling of R- and Mn-spin order is reflected in $\tau^{\mathrm{R}} = \tau^{\mathrm{Mn}}$, a behavior that is now confirmed for R = Tb, Dy and Ho [13, 15, 16]. R = Ho represents the strong coupling regime as $\tau^{\mathrm{Mn}} = \tau^{\mathrm{Ho}}$ is preserved to the lowest temperatures [13, 23]. Our model also reproduces the behavior for R = Dy for a weak coupling regime as we recover the commensurate $\tau^{\mathrm{Dy}} = 1/2$ ordering [16, 20]. However, the case of R = Tb is more interesting as it represents an intermediate coupling regime with complex behavior. In particular, below $T_{\mathrm{N}}^{\mathrm{Tb}}$, when $J_{\mathrm{Tb-Tb}}$ becomes important, we find that the Tb and Mn orderings remain coupled through the matching of their wavevectors, $3\tau^{\mathrm{Tb}} - \tau^{\mathrm{Mn}} = 1$.

## 4. Enhancement of the ferroelectric polarization by R-spin ordering

A critical question that emerges for the ferroelectric properties of the $RMnO_3$ perovskites is if the ordering of R-spins can directly or indirectly affect the multiferroic behavior. While it is clear that the magnetic anisotropy provided by R-spins facilitates the flop of the polarization from the *c*- to the *a*-axis in an applied field [17], its effect on the magnitude of the polarization has not been considered. Motivated by the anomalous behavior of the polarization for R = Dy compared to R = Tb, we have shown that the clamping of the R-spins to Mn-spin order can indeed lead to an enhancement of the ferroelectric polarization [20].

More specifically for R = Dy in the region just above $T_{\mathrm{N}}^{\mathrm{Dy}}$, the electric polarization is three times larger for R = Dy compared to R = Tb and shows a large hysteresis [5] with almost a 50% difference in $P_{\mathrm{s}}$ obtained after cooling to 2 and 7 K, respectively (see figure 8(a)). Single crystal XRMS showed incommensurate Dy induced magnetic ordering with the same periodicity as the Mn one below $T_{\mathrm{S}}$ (see figure 8(c)) [20]. The commensurate Dy ordering below $T_{\mathrm{N}}^{\mathrm{Dy}}$ results in an abrupt decrease in $P_{\mathrm{s}}$, while the commensurate to incommensurate transition shows a large hysteresis in which $P_{\mathrm{s}}$ and the intensity of incommensurate Dy magnetic scattering exhibit a similar behavior. All these

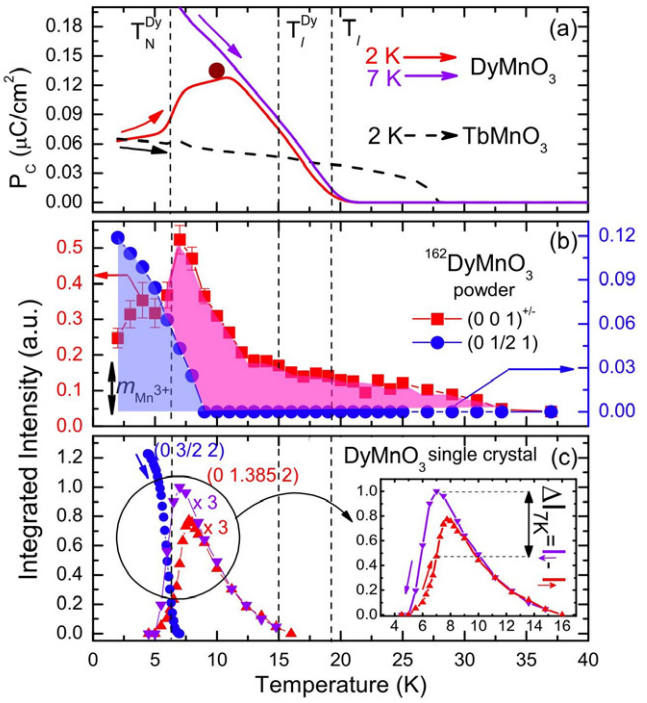


**Figure 8.** Temperature dependences of (a) electric polarization along the $c$-axis for $DyMnO_3$ and $TbMnO_3$ (from Goto *et al* [5]), (b) integrated (neutron) intensities of magnetic A-type and $(0\ \frac{1}{2}\ 1)$ reflections measured on heating ($\updownarrow m_{Mn^{3+}}$ shows the intensity corresponding to a 4 $\mu_B$ $Mn^{3+}$ magnetic moment for this reflection), (c) temperature dependent integrated (synchrotron) intensities of selected Dy commensurate (heating) and incommensurate (heating and cooling) superlattice reflections. The region around $T_N^{Dy}$ is shown in the insert. Here, $\Delta I$ highlights the difference between intensities on cooling and heating at 7 K. The symbol ● in panel (a) represent the prediction of $P$ at 10 K for R = Dy on the basis of the ordering of both Mn- and Dy-spins determined by neutron diffraction (see text).

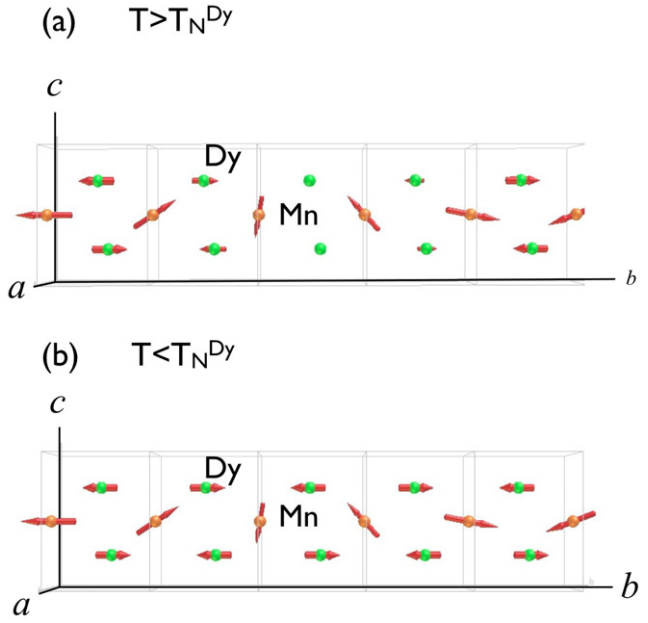


**Figure 9.** Illustration of the magnetic ordering of Dy- and Mn-spins in the $bc$-plane (a) at temperatures above and (b) below $T_N^{Dy}$.

facts point to the direct effect of R-magnetism on the electric polarization.

Neutron diffraction measurements of a powder sample of R = $^{162}$Dy showed an increase in the intensity of $\tau^{Mn}$ reflections below $T_N$, but with further cooling below $T_S$ = 15 K, the intensity of these reflections increases more rapidly (see figure 8(b)). At $T_N^{Dy}$ however, the intensity of $\tau^{Mn}$ rapidly decreases while $\tau^{Dy} = (1/2)\mathbf{b}^*$ reflections appear as also found in the XRMS measurements in figures 8(b) and (c). Rietveld analysis of the NPD data between $T_N^{Dy} < T < 13$ K on the assumption of pure Mn-spin-ordering lead to unphysically large moments for $Mn^{3+}$ (>4 $\mu_B$/Mn) (figure 5(b)). Using the XRMS information we can construct a reliable model for the magnetic structure of $DyMnO_3$. For the Mn-spins we use the $bc$-cycloidal model as indicated, with the spontaneous polarization along the $c$-axis, while the R moments are allowed to have components along the three principal crystallographic directions denoted as $\mathbf{m}^{Dy} = (a_x, f_y, f_z)$ [23], consistent with the $\Gamma_2 \times \Gamma_3$ irreducible representation for the Mn-spin-ordering [15]. Our Rietveld analysis shows that the magnetic moment is $\mathbf{m}^{Dy} = (0.4(6), 2.5(2), 0.0(3))$ $\mu_B$/Dy. The ordering of Dy- and Mn-spins projected onto the $bc$-plane is shown in figure 9(a). The maximum value of the moment here is approximately twice as much as that found for the induced moment of Tb in $TbMnO_3$ ($\mathbf{m}^{Tb} = (1.2, 0, 0)$ $\mu_B$/Tb [15]). For the commensurate phase below $T_N^{Dy}$ Rietveld shows that the Dy moments with absolute value $m^{Dy} = 6.2(6)$ $\mu_B$/Dy lie in the $ab$ plane as shown in figure 9(b) [20].

From this analysis it is clear that the sinusoidal ordering of Dy-spins above $T_N^{Dy}$ cannot cause a ferroelectric polarization of the lattice, so a simple additive mechanism $P = P_{Mn} + P_{Dy}$ can be excluded. A simple way to quantitatively account for the enhanced polarization just above $T_N^{Dy}$ is to consider phenomenologically the magneto-electric coupling resulting from the interplay between the Mn cycloid and R-spins, which can be described using the continuum model of the type considered in [17]. The relevant antiferromagnetic order parameters are $\mathbf{L} = \mathbf{S}_1 + \mathbf{S}_2 - \mathbf{S}_3 - \mathbf{S}_4$, for manganese spins as well as $\mathbf{R}_1 = \mathbf{S}_5 + \mathbf{S}_6 + \mathbf{S}_7 + \mathbf{S}_8$ and $\mathbf{R}_2 = \mathbf{S}_5 - \mathbf{S}_6 + \mathbf{S}_7 - \mathbf{S}_8$, for R-spins (the labeling of spins in the unit cell is the same as in [35]). The transformation properties of various components of these order parameters under the symmetry transformations of the $Pbnm$ group are shown in table 2. The coupling of the spiral ordering of manganese spins to electric polarization is described by the invariant combination [17];

$$F_{Mn-Mn} = -\lambda P^z (L^z \overleftrightarrow{\partial_y} L^y), \tag{2}$$

where $A \overleftrightarrow{\partial_y} B = A\partial_y B - B\partial_y A$, while the interplay between the $x$ and $y$ components of the rare earth spins and the $y$ component of the manganese spins is described by

$$F'_{Mn-R} = -\lambda' P^z (R_1^y \overleftrightarrow{\partial_y} L^y) \tag{3}$$

and

$$F''_{Mn-R} = -\lambda'' P^z (R_2^x \overleftrightarrow{\partial_y} L^y). \tag{4}$$

**Table 2.** The transformation properties of components of the two antiferromagnetic order parameters, electric polarization and the gradient upon the symmetry operations of the *Pbnm* group.

| | $m_x$ | $m_y$ | $m_z$ | $2_x$ | $2_y$ | $2_z$ | $\mathcal{I}$ |
|---|---|---|---|---|---|---|---|
| $L^x$ | + | + | + | + | + | + | + |
| $L^y$ | − | − | + | − | − | + | + |
| $L^z$ | − | + | − | − | + | − | + |
| $R_1^x$ | + | − | − | + | − | − | + |
| $R_1^y$ | − | + | − | − | + | − | + |
| $R_1^z$ | − | − | + | − | − | + | + |
| $R_2^x$ | − | + | − | − | + | − | + |
| $R_2^y$ | + | − | − | + | − | − | + |
| $R_2^z$ | + | + | + | + | + | + | + |
| $P^z$ | + | + | − | − | − | + | − |
| $\partial_y$ | + | − | + | − | + | − | − |

The order parameter $L^y$ transforms according to the $\Gamma_3$ representation, while $L^z$, $R_1^y$, and $R_2^x$ belong to $\Gamma_2$, in agreement with the symmetry analysis of [35]. As long as the modulations of the R- and Mn-spins have the same wavevector, the coupling equations (3) and (4) give an additional contribution to the magnetically induced polarization. The decrease in $P_s$ below $T_N^{Dy}$ we ascribe to the change in the wavevector for the Dy ordering ($\tau^{Dy} \neq \tau^{Mn}$) as illustrated in figure 8(a).

Why is the observed enhancement in $P_s$ for R = Dy much larger compared to that for R = Tb? Although equations (2), (3) and (4), describing the Mn–Mn and R–Mn magneto-electric coupling look similar, the underlying microscopic mechanisms may be very different. Using the table 2 one can check that the magneto-electric coupling term involving both manganese and rare earth spins, $-\lambda'_\alpha P^z (L_R^\alpha \overleftrightarrow{\partial_y} L_{Mn}^\alpha)$, is invariant upon all the symmetry transformations for *any* spin projection $\alpha = x, y, z$. This suggests that it might be nonzero even in absence of magnetic anisotropies, in which case it would have a rotationally invariant form:

$$F'_{Mn-R} = -\lambda' P^z \left( \mathbf{R}_1 \cdot \overleftrightarrow{\partial_y} \mathbf{L} \right). \tag{5}$$

Since manganese spins in neighboring layers have opposite orientations and rare earth spins reside right in between the layers, one can argue that Mn- and R-spin subsystems only become exchange coupled in the ferroelectric state, when the electric polarization $P^z$ breaks the mirror $m_z$, which would give rise to the magneto-electric coupling equation (5).

On the other hand, the coupling equation (2), inducing the polarization in the cycloidal spiral state of Mn-spins, is strongly anisotropic and has a relativistic origin [36, 37]. This may explain why the anisotropic magneto-electric coupling equation (4) of the Tb-spins, which have a strong $a$-component, is much weaker than the coupling equation (3) of the Dy-spins with the largest component along the $b$-axis parallel to one of the components of the Mn spiral.

Guided by the above arguments we can use our experimental determination of the magnetic structure of $DyMnO_3$ to compute the ferroelectric polarization just above $T_N^{Dy}$. Since in the ferroelectric phase the relevant irreducible representation that describes the magnetic ordering is $\Gamma_2 \times \Gamma_3$ and the Dy-spins are clamped to the Mn-spins ($\tau^{Dy} = \tau^{Mn}$), the Dy ordering can be written as $M^{Dy} = m_y^{Dy} \cos(\boldsymbol{\tau} \cdot \mathbf{y})$, where $\mathbf{y}$ is a unit vector along the $b$-axis. Here we couple $m_y^{Dy}$ to the $c$-axis component of the Mn cycloid (see above) and following reference [17] we have $\mathbf{P}_s = \gamma \chi m_y^{Mn} (m_z^{Mn} + \epsilon m_y^{Dy})(\mathbf{e_x} \times \boldsymbol{\tau})$, where $\gamma$ and $\chi$ are a coupling constant and the susceptibility respectively. Comparing the values of $P_s$ for R = Tb and Dy we can estimate the value of the polarization for $DyMnO_3$ on the basis of $m_y^{Mn}$, $m_z^{Mn}$ and $m_y^{Dy}$ determined from the analysis of the neutron diffraction data just above $T_N^{Dy}$. Taking the values of the magnetic moments for R = Tb from [15] and for R = Dy from this work and choosing $\epsilon = 1$ we have a value of $P^{Tb} = 3.1\gamma\chi$ and $P^{Dy} = 7.9\gamma\chi$. Scaling these values to $P^{Tb}(10\ K) \sim 0.055\ \mu C\ m^{-2}$, we can compute $P^{Dy}(10\ K) = 0.14\ \mu C\ m^{-2}$, in excellent agreement with the experimental measurements shown in figure 8(a), assuming the constants are equal in both compounds.

## 5. Summary

In conclusion we have shown that the magnetic ordering in $RMnO_3$ multiferroic perovskites with magnetic R-ions can be complex and different scattering techniques are required to de-convolute the ordering of both magnetic species. Our investigation of the magnetic structure of $TbMnO_3$ shows that the Mn magnetic ordering is described essentially by the A-mode which is polarized in the $bc$-plane. A smaller Mn-spin component along the $a$-axis is indicated by the G-mode. We find that Tb-spins at 12 K above $T_N^{Tb}$ order in the $ac$-plane where $m_x^{Tb} > m_z^{Tb}$. This ordering is reflected by the C-, F- and G-modes. The induced ordering of Tb-spins can be easily suppressed in favor of a ferromagnetic ordering with a magnetic field applied along the $a$-axis.

While neutron diffraction as well as polarized neutron techniques are very powerful, the use of element specific methods such as XRMS has proven to be invaluable in directly observing the induced ordering of R-spins. Our measurements have shown that an induced ordering of R-spins that appears below $T_S$ results in magnetic structures where both R- and Mn-spins order with the same periodicity. For $DyMnO_3$, Dy-spins order independently with a wavevector of $\tau^{Dy} = (1/2)\mathbf{b}^*$ below $T_N^{Dy}$. However for R = Tb, we find that the clamping between the Mn and Tb sublattice is maintained and that $\tau^{Tb}$ and $\tau^{Mn}$ lock-in to rational values of $(3/7)\mathbf{b}^*$ and $(2/7)\mathbf{b}^*$. This behavior in zero field for R = Tb as well as the shift of $\tau^{Tb}$ and $\tau^{Mn}$ to values close to the rational fractions 4/11 and 3/11 respectively under magnetic field, demonstrated the richness in magneto-elastic behavior that can be obtained from the interplay of R- and Mn-spins. The theoretical framework we have presented here based on the frustrated ANNNI model not only explains the behavior for R = Tb but can also account for the independent ordering for R = Dy below $T_N^{Dy}$ in terms of a stronger coupling between Dy-spins. While the importance of $J_{Mn-R}$ has been highlighted in understanding the magnetic ordering in R = Tb, its relevance to multiferroics properties

is demonstrated in the case of R = Dy. Thus we showed that the clamped ordering of Dy- and Mn-spins can enhance the ferroelectric polarization, as long as the Dy order effectively adds to one of the components of the Mn cycloid. This leads to the possibility of using the induced ordering of R-spins to engineer multiferroics with higher ferroelectric polarization.

## Acknowledgments

The authors thank M Meissner, K Kiefer and S Gerischer from BENSC for their assistance with the sample environment during the neutron measurements. We also thank J Hoffmann and U Amann for their assistance during our measurements on the E2 diffractometer. We have benefited from discussions with M Braden, D Senff and D Khomskii. We thank D Senff for his help with figure 1. DNA thanks the Deutschen Forschungsgemeinschaft for financial support under contract AR-613/1-1.

## References

[1] Fiebig M 2005 *J. Phys. D: Appl. Phys.* **38** R123
[2] Hill N 2000 *J. Phys. Chem.* B **104** 6694
[3] Gregoire P S, Almairac R and Gesland J 1986 *Ferroelectrics* **67** 15
[4] Cheong S-W and Mostovoy M 2007 *Nat. Mater.* **6** 13
[5] Goto T, Kimura T, Lawes G, Ramirez A P and Tokura Y 2004 *Phys. Rev. Lett.* **92** 257201
[6] Kimura T, Lawes G, Goto T, Tokura Y and Ramirez A P 2005 *Phys. Rev.* B **71** 224425
[7] Kimura T, Goto T, Shintani H, Ishizaka K, Arima T and Tokura Y 2003 *Nature* **426** 55
[8] Hur N, Park S, Sharma P A, Ahn J S, Guha S and Cheong S-W 2004 *Nature* **429** 392
[9] Yamasaki Y, Miyasaka S, Kaneko Y, He J, Arima T and Tokura Y 2006 *Phys. Rev. Lett.* **96** 207204
[10] Kimura T, Ishihara S, Shintani H, Arima T, Takahashi K T, Ishizaka K and Tokura Y 2003 *Phys. Rev.* B **68** 060403
[11] Goodenough J 1955 *Phys. Rev.* **100** 564
[12] Senff D, Link P, Hradil K, Hiess A, Regnault L P, Sidis Y, Aliouane N, Argyriou D N and Braden M J 2007 *Phys. Rev. Lett.* **98** 137206
[13] Muñoz A, Casáis M T, Alonso J A, Martínez-Lope M J, Martínez J L and Fernández-Díaz M T 2001 *Inorg. Chem.* **40** 1020
[14] Kajimoto R, Yoshizawa H, Shintani H, Kimura T and Tokura Y 2004 *Phys. Rev.* B **70** 012401
[15] Kenzelmann M, Harris A B, Jonas S, Broholm C, Schefer J, Kim S B, Zhang C L, Cheong S-W, Vajk O P and Lynn J W 2005 *Phys. Rev. Lett.* **95** 087206
[16] Feyerherm R, Dudzik E, Aliouane N and Argyriou D N 2006 *Phys. Rev.* B **73** 180401
[17] Mostovoy M 2006 *Phys. Rev. Lett.* **96** 067601
[18] Katsura H, Nagaosa N and Balatsky A V 2005 *Phys. Rev. Lett.* **95** 057205
[19] Prokhnenko O, Feyerherm R, Mostovoy M, Aliouane N, Dudzik E, Wolter A U B, Maljuk A and Argyriou D N 2007 *Phys. Rev. Lett.* **99** 177206
[20] Prokhnenko O, Feyerherm R, Dudzik E, Landsgesell S, Aliouane N, Chapon L C and Argyriou D N 2007 *Phys. Rev. Lett.* **98** 057206
[21] Quezel S, Tcheou F, Rossat-Mignod J, Quezel G and Roudaut E 1977 *Physica* B+C **86–88** 916
[22] Bertaut E F 1981 *J. Magn. Magn. Mater.* **24** 267
[23] Brinks H W, Rodríguez-Carvajal J, Fjellvåg H, Kjekshus A and Hauback B C 2001 *Phys. Rev.* B **63** 094411
[24] Voigt J, Persson J, Kim J W, Bihlmayer G and Brueckel T J 2007 *Phys. Rev.* B **76** 104431
[25] Schärpf O and Chapellmann H 1990 *Z. Phys.* B **80** 253
[26] Schärpf O and Chapellmann H 1993 *Phys. Status Solidi* a **135** 359
[27] Lorenz B, Wang Y Q, Sun Y Y and Chu C W 2004 *Phys. Rev.* B **70** 212412
[28] Feyerherm R 2007 unpublished
[29] Arima T, Goto T, Yamasaki Y, Miyasaka S, Ishii K, Tsubota M, Inami T, Murakami Y and Tokura Y 2005 *Phys. Rev.* B **72** 100102(R)
[30] Cashion J D and Wells M R 1998 *J. Magn. Magn. Mater.* **177–181** 781
[31] Mannix D, McMorrow D, Ewings R, Boothroyd A, Prabhakaran D, Joly Y, Janousova B, Mazzoli C, Paolasini L and Wilkins S 2007 *Phys. Rev.* B **76** 184420
[32] Aliouane N, Argyriou D N, Strempfer J, Zegkinoglou I, Landsgesell S and v Zimmermann M 2006 *Phys. Rev.* B **73** 020102(R)
[33] Bielen J, Marescha J and Sivardie J 1967 *Z. Angew. Phys.* **23** 243
[34] Bouree J and Hammann J 1975 *J. Physique* **36** 391
[35] Harris A B 2007 *Phys. Rev.* B **76** 054447
[36] Sergienko I A, Şen C and Dagotto E 2006 *Phys. Rev. Lett.* **97** 227204
[37] Sergienko I A and Dagotto E 2006 *Phys. Rev.* B **73** 094434